Commun. Comput. Phys.
doi: 10.4208/cicp.290914.030615a

Vol. **19**, No. 3, pp. 603-631
March 2016

Development of a Combined Compact Difference Scheme to Simulate Soliton Collision in a Shallow Water Equation

Ching-Hao Yu[1] and Tony Wen-Hann Sheu[2,3,4,*]

[1] *Ocean College, Zhejiang University, 866 Yuhangtang Road, Hangzhou, Zhejiang, China.*
[2] *Department of Engineering Science and Ocean Engineering, National Taiwan University, No. 1, Sec. 4, Roosevelt Road, Taipei, Taiwan.*
[3] *Institute of Applied Mathematical Sciences, National Taiwan University, Taipei, Taiwan.*
[4] *Center of Advanced Study in Theoretical Sciences (CASTS), National Taiwan University, Taipei, Taiwan.*

Communicated by Wei Shyy

Received 29 September 2014; Accepted (in revised version) 3 June 2015

Abstract. In this paper a three-step scheme is applied to solve the Camassa-Holm (CH) shallow water equation. The differential order of the CH equation has been reduced in order to facilitate development of numerical scheme in a comparatively smaller grid stencil. Here a three-point seventh-order spatially accurate upwinding combined compact difference (CCD) scheme is proposed to approximate the first-order derivative term. We conduct modified equation analysis on the CCD scheme and eliminate the leading discretization error terms for accurately predicting unidirectional wave propagation. The Fourier analysis is carried out as well on the proposed numerical scheme to minimize the dispersive error. For preserving Hamiltonians in Camassa-Holm equation, a symplecticity conserving time integrator has been employed. The other main emphasis of the present study is the use of $u-P-\alpha$ formulation to get non-dissipative CH solution for peakon-antipeakon and soliton-anticuspon head-on wave collision problems.

AMS subject classifications: 35L05, 35J05, 65M06

Key words: Camassa-Holm equation, seventh-order spatially accurate, CCD, symplecticity, peakon-antipeakon, soliton-anticuspon.

*Corresponding author. *Email addresses:* chyu@zju.edu.cn (C.-H. Yu), twhsheu@ntu.edu.tw (T. W.-H. Sheu)

1 Introduction

Many weakly nonlinear dispersive partial differential equations have been known to permit soliton solutions [1]. Complex interaction amongst solitons in these physical systems has attracted considerable attention in the past. Soliton discovered experimentally by Russel is defined as a single humped wave of bulge water. Take the Korteweg-de Vries (KdV) equation $u_t+6uu_x+u_{xxx}=0$ as an example, solitary wave is formed due to the balance between the weak nonlinear steepening effect of uu_x and the linear dispersion effect of u_{xxx}. The nonlinear term in this equation tends to steepen the solution but the dispersion term is prone to spread it out at the same time. These localized and highly stable solitons amenable to KdV equation can retain its identity upon interaction. Because of the ability of preserving wave shape and speed, the collision of KdV solutions is classified to be of an elastic type.

Besides the celebrated KdV equation, the completely integrable Camassa-Holm (CH) equation [2] has also received considerable attention in the past two decades. Provided that an initial data is defined in the Sobolev space $H^s(\Omega)$ for $s>\frac{3}{2}$, CH equation is locally well-posed [3]. The reason for investigating this Cauchy problem is rooted in its possession of a rich geometric solution structure. Camassa-Holm equation investigated under a permanent wave motion has a global strong solution. In addition, this equation permitting blow-up solution can be used to model wave breaking [3]. For an initial data of the $H^1(\mathcal{R})$ type, Camassa-Holm equation is also amenable to global weak solution [4].

A smooth solution of CH equation can be compressed to form a jump in the solution in finite time [2] due to the occurrence of nonlinear terms in CH equation. In the presence of peakon solution, the CH solution computed at $\kappa=0$ exhibits a discontinuous first derivative at the crest. Any numerically introduced high-frequency dispersion error near these peaks can considerably deteriorate simulation quality [5]. It is natural to apply a compact scheme [6] to get a better understanding of the nonlinear and dispersive natures. In addition, the Weighted Essentially Non-Oscillatory (WENO) scheme [7] is also desired to avoid the oscillatory solutions.

Application of the finite difference scheme in [8] can properly model the peakon-antipeakon interaction. The pseudospectral scheme developed by Kalisch and Lenells [9] has been shown to be effective in predicting the solution of CH equation. Peakon solutions have been predicted more correctly by Artebrant and Schroll [10] using the adaptive upwinding finite volume discretization method. One can also apply the local discontinuous Galerkin method to predict the CH solution [5]. In addition to the above-mentioned methods, multi-symplectic method [11], energy-conserving Galerkin method [12], Hamiltonian-conserving Galerkin method [13] and self-adaptive mesh method [8] have been also developed to solve the CH equation with great success.

The rest of this paper is organized as follows. Section 2 describes the nonlinear CH equation and its remarkable mathematical features. This equation containing the third-order derivative term is then transformed to its equivalent nonlinear system of equations. This equivalent differential system of equations consists of one equation with the reduced

differential order and one inhomogeneous Helmholtz equation. In the first step of the solution algorithm, the nonlinear advection equation is numerically approximated by the combined compact difference scheme detailed in Section 4.2. We then present a sixth-order accurate scheme for solving the inhomogeneous Helmholtz equation in Section 4.5. Section 5 is devoted to the dispersion analysis of the proposed seventh-order accurate CCD scheme. In Section 6.1 the solution of CH equation will be sought under different initial conditions to elucidate the symplecticity-preserving scheme property proposed in this manuscript. This scheme containing only a minimal numerical phase error has been applied to predict the propagation of peakons and antipeakon. We examine interaction between peakons and antipeakon in detail and conclude that the peakon-antipeakon collision is indeed elastic in the sense of retaining conservation property. In Section 6.2, the CH equation is solved for $\kappa \neq 0$ to justify the applicability of the proposed spatially seventh-order accurate upwinding difference scheme in capturing the traveling wave nature. Interactions between peakons, peakon-antipeakon, and solition-anticuspon are also numerically investigated. Finally, we will draw some concluding remarks in Section 7.

2 Working equation

The nonlinear Camassa-Holm (CH) equation derived as follows in [2]

$$u_t+2\kappa u_x-u_{xxt}+3uu_x=2u_xu_{xx}+uu_{xxx} \tag{2.1}$$

will be studied here. For the case of non-negative real κ $(\equiv (gh_0)^{1/2})$, g stands for the gravity and h_0 denotes the undisturbed water depth. In the limit $\kappa=0$, Eq. (2.1) turns out to be the special case of the b-family partial differential equation $u_t-u_{xxt}+(b+1)\,uu_x=bu_xu_{xx}+uu_{xxx}$ for $b=2$ [14]. When $b=3$, this equation is known as the Degasperis-Procesi equation [15, 16].

The nonlinear term uu_x in CH equation can steepen wave. The presence of the nonlinear dispersion term uu_{xxx} rather than the linear dispersion term κu_x in KdV equation results in a complex wave spreading. The above two competing terms considered together with the nonlinear term u_xu_{xx} and the space-time mixed derive term u_{xxt} in the CH equation for $\kappa=0$ admit peakon solution which is represented by a piecewise function.

Peakon (or peaked soliton) solution for the CH equation investigated at $\kappa=0$ can be represented as $u(x,t)=c\ e^{-|x-ct|}$. If c is a negative quality, the wave with its peak pointing downward propagates towards left. This peaked solution is often called as an antipeakon, which is in contrast to the right-running peakon for which $c>0$. At wave crest this solution slope has a finite discontinuity [2]. The interaction of these peakons and antipeakons generates many dynamically interesting features. These intriguing behaviors are normally scarce in their piecewise soliton counterparts, thereby prompting the present study. For $\kappa\neq 0$, the dispersive term $2\kappa u_x$ can further steepen the

peakon/antipeakon solution. Eq. (2.1) admits cusped soliton, known as the cuspon, as well as the smooth soliton solution [8].

CH equation can be completely integrated through its associated Lax pair. Since CH equation has a multi-symplectic structure, Eq. (2.1) can be rewritten as a system of first-order equations given by $\underline{\underline{M}}\ \underline{z}_t+\underline{\underline{K}}\ \underline{z}_x=\nabla_z S(z)$ for a state-variable vector $\underline{z}$. The scalar function S is smoothly dependent on $\underline{z}$. The skew-symmetric square matrices $\underline{\underline{M}}$ and $\underline{\underline{K}}$ define the symplectic structure given by $(\overline{\omega},\overline{\kappa})$, where $\overline{\omega}=d\underline{z}\wedge\underline{\underline{M}}d\underline{z}$ and $\overline{\kappa}=d\underline{z}\wedge\underline{\underline{K}}d\underline{z}$. According to the work of Bridges and Reich [17], the pair of variables $(\overline{\omega},\overline{\kappa})$ conserves symplecticity locally by way of $\frac{\partial\overline{\omega}}{\partial t}+\frac{\partial\overline{\kappa}}{\partial x}=0$. Some of the differential conservation laws and the integrable conserved quantities have been derived in [11].

Given an initial condition $u_0(x,\ t=0)\in H^1$, where H^1 is the Sobolev space, equation (1) investigated at $\kappa=0$ has been shown to possess the well-known conservation laws $\int_{-\infty}^{+\infty}u\ dx$. (H_0), $\frac{1}{2}\int_{-\infty}^{+\infty}(u^2+u_x^2)\ dx$ (Hamiltonian H_1) and $\frac{1}{2}\int_{-\infty}^{+\infty}(u^3+uu_x^2+2\kappa u^2)\ dx$ (Hamiltonian H_2). Note that $H_1=\frac{1}{2}\int_{-\infty}^{+\infty}(u^2+u_x^2)\ dx$ has association with the energy density $u^2+u_x^2$ [18].

3 $u-P-\alpha$ formulation for the CH equation

When approximating CH equation, it is generally accepted to avoid dealing with the less understood third-order derivative term and the mixed space-time derivative term. To this end, the original third-order CH equation is transformed first to its equivalent set of equations containing only the first-order spatial and the temporal derivative terms by introducing two auxiliary variables. Choice of the momentum variable $m=u-u_{xx}$ led us to get the following $u-m$ formulation [19]

$$m_t+um_x+2u_xm=-2\kappa u_x. \tag{3.1}$$

One can also transform the original CH equation to get the other equivalent set of $u-P$ equations [20]

$$u_t+uu_x=-P_x, \tag{3.2}$$

$$P-P_{xx}=u^2+\frac{1}{2}(u_x)^2+2\kappa u. \tag{3.3}$$

The solutions of the above two sets of $u-m$ and $u-p$ equations are sought subject to the prescribed periodic boundary condition. Through the previous computational assessment study, we know that the $u-P$ formulation is superior to the $u-m$ formulation [20].

To avoid computing the term $(u_x)^2$ in the inhomogeneous Helmholtz equation (3.3), we should replace $(u_x)^2$ by a term, such as the Hamiltonian H_2, that is continuous even at a jump of wave crest. In this light, the following energy density is taken into account in the current reformulation of the CH equation [11]

$$\alpha=u^2+(u_x)^2. \tag{3.4}$$

One can then easily derive the following transport equation for α in conservative form

$$\alpha_t+(u\alpha)_x=-Q_x, \tag{3.5}$$

where $Q=2Pu-u^3-2\kappa u^2$. The $u-P-\alpha$ formulation employed in this study is as follows

$$u_t+uu_x=-P_x, \tag{3.6}$$

$$P-P_{xx}=\frac{u^2}{2}+\frac{\alpha}{2}+2\kappa u, \tag{3.7}$$

$$\alpha_t+(u\alpha)_x=-Q_x. \tag{3.8}$$

To get a better understanding of the nonlinear and dispersive natures of the shallow water, Eqs. (3.6)-(3.8) constitutes an appropriate differential system for us to design a numerical scheme.

4 Numerical schemes

In this study the classical semi-discretization method is adopted to approximate the time-dependent differential equation (3.6). The time derivative term is approximated before approximating the spatial derivative terms.

4.1 Symplectic scheme for the temporal derivative term

When solving the Hamiltonian equation (2.1), a structure-preserving numerical integrator should be adopted to conserve its symplecticity. The sixth-order accurate symplectic Runge-Kutta scheme [21] is used in this study to get a long-time accurate CH solution

$$u^{(1)}=u^n+\Delta t\left[\frac{5}{36}F^{(1)}+(\frac{2}{9}+\frac{2\tilde{c}}{3})F^{(2)}+(\frac{5}{36}+\frac{\tilde{c}}{3})F^{(3)}\right], \tag{4.1}$$

$$u^{(2)}=u^n+\Delta t\left[(\frac{5}{36}-\frac{5\tilde{c}}{12})F^{(1)}+(\frac{2}{9})F^{(2)}+(\frac{5}{36}+\frac{5\tilde{c}}{12})F^{(3)}\right], \tag{4.2}$$

$$u^{(3)}=u^n+\Delta t\left[(\frac{5}{36}-\frac{\tilde{c}}{3})F^{(1)}+(\frac{2}{9}-\frac{2\tilde{c}}{3})F^{(2)}+\frac{5}{36}F^{(3)}\right], \tag{4.3}$$

$$u^{n+1}=u^n+\Delta t\left[\frac{5}{18}F^{(1)}+\frac{4}{9}F^{(2)}+\frac{5}{18}F^{(3)}\right]. \tag{4.4}$$

where $\tilde{c}=\frac{1}{2}\sqrt{\frac{3}{5}}$. Note that $F^{(i)}$ $(i=1,2,3)$ shown above represent the values of $F(\equiv -P_x-uu_x)$ at $t=n+(\frac{1}{2}+\tilde{c})\Delta t$, $t=n+\frac{1}{2}\Delta t$, and $t=n+(\frac{1}{2}-\tilde{c})\Delta t$, respectively.

4.2 Combined compact difference scheme for spatial derivative terms

To get a long-time accurate CH solution, one can employ the DRP (dispersion-relation-preserving) scheme given in [22]. In this study, the compact difference scheme [23] is implemented in a grid stencil having three points.

We propose first the combined compact difference scheme for the first-order derivative term. The derivation detail is presented below. The derivative terms u_x, u_{xx} and u_{xxx} at each grid point are all considered as the solution variables so as to get the spectral-like resolution. The proposed non-centered or upwinding combined compact difference scheme formulated in a three-point grid stencil for the derivative terms $\frac{\partial u}{\partial x}$, $\frac{\partial^2 u}{\partial x^2}$ and $\frac{\partial^3 u}{\partial x^3}$ is given as

$$\frac{\partial u}{\partial x}\Big|_i + a_1 \frac{\partial u}{\partial x}\Big|_{i-1} + h\left(b_1 \frac{\partial^2 u}{\partial x^2}\Big|_{i-1} + b_2 \frac{\partial^2 u}{\partial x^2}\Big|_i + b_3 \frac{\partial^2 u}{\partial x^2}\Big|_{i+1}\right) + h^2\left(c_1 \frac{\partial^3 u}{\partial x^3}\Big|_{i-1} + c_3 \frac{\partial^3 u}{\partial x^3}\Big|_{i+1}\right) = \frac{1}{h}(d_1 u_{i-1} + d_2 u_i + d_3 u_{i+1}), \tag{4.5}$$

$$\frac{\partial^2 u}{\partial x^2}\Big|_i + \frac{1}{h}\left(-\frac{29}{16}\frac{\partial u}{\partial x}\Big|_{i-1} + \frac{29}{16}\frac{\partial u}{\partial x}\Big|_{i+1}\right) + \left(-\frac{5}{16}\frac{\partial^2 u}{\partial x^2}\Big|_{i-1} - \frac{5}{16}\frac{\partial^2 u}{\partial x^2}\Big|_{i+1}\right) + h\left(-\frac{1}{48}\frac{\partial^3 u}{\partial x^3}\Big|_{i-1} + \frac{1}{48}\frac{\partial^3 u}{\partial x^3}\Big|_{i+1}\right) = \frac{1}{h^2}(4u_{i-1} - 8u_i + 4u_{i+1}), \tag{4.6}$$

$$\frac{\partial^3 u}{\partial x^3}\Big|_i + \frac{1}{h^2}\left(-\frac{105}{16}\frac{\partial u}{\partial x}\Big|_{i-1} - \frac{105}{16}\frac{\partial u}{\partial x}\Big|_{i+1}\right) + \frac{1}{h}\left(-\frac{15}{8}\frac{\partial^2 u}{\partial x^2}\Big|_{i-1} + \frac{15}{8}\frac{\partial^2 u}{\partial x^2}\Big|_{i+1}\right) + \left(-\frac{3}{16}\frac{\partial^3 u}{\partial x^3}\Big|_{i-1} - \frac{3}{16}\frac{\partial^3 u}{\partial x^3}\Big|_{i+1}\right) = \frac{1}{h^3}\left(\frac{105}{16}u_{i-1} - \frac{105}{16}u_{i+1}\right). \tag{4.7}$$

The second-order derivative term $\frac{\partial^2 u}{\partial x^2}$ and the third-order derivative term $\frac{\partial^3 u}{\partial x^3}$ at an interior node i are approximated using the centered schemes. The coefficients shown in (4.6)-(4.7) are determined through the Taylor series expansion with respect to u_i. Their respective leading truncation error terms in the derived modified equations are then eliminated. The resulting formal solution accuracies for $\frac{\partial^2 u}{\partial x^2}$ and $\frac{\partial^3 u}{\partial x^3}$ become eighth-order and sixth-order, respectively [24].

The proposed upwinding compact difference scheme is derived only for the case of $u > 0$. Derivation for the negative coefficient case can be done likewise. In order to estimate the eight weighting coefficients shown in (4.5) we start with the Taylor series expansion of the terms u_{i-1}, u_{i+1}, $\frac{\partial u}{\partial x}|_{i-1}$, $\frac{\partial u}{\partial x}|_i$, $\frac{\partial^2 u}{\partial x^2}|_{i-1}$, $\frac{\partial^2 u}{\partial x^2}|_i$, $\frac{\partial^2 u}{\partial x^2}|_{i+1}$, $\frac{\partial^3 u}{\partial x^3}|_{i-1}$, and $\frac{\partial^3 u}{\partial x^3}|_{i+1}$ with respect to u_i and then eliminate the leading error terms shown in the modified equation for $\frac{\partial u}{\partial x}$. The resulting set of algebraic equations is as follows

$$d_1 + d_2 + d_3 = 0, \tag{4.8}$$

$$-a_1 - d_1 + d_3 = 1, \tag{4.9}$$

$$2a_1+d_1+d_3-2b_1-2b_2-2b_3=0, \tag{4.10}$$
$$d_1-d_3-6b_1+6b_3+6c_1+6c_3+3a_1=0, \tag{4.11}$$
$$d_1+d_3-12b_1-12b_3+24c_1-24c_3+4a_1=0, \tag{4.12}$$
$$d_1-d_3-20b_1+20b_3+60c_1+60c_3+5a_1=0, \tag{4.13}$$
$$d_1+d_3-30b_1-30b_3+120c_1-120c_3+6a_1=0, \tag{4.14}$$
$$d_1-d_3-42b_1+42b_3+210c_1+210c_3+7a_1=0. \tag{4.15}$$

We are still lack of one algebraic equation to uniquely determine all the nine introduced coefficients shown in (4.5). The wave-type error will be minimized or the dispersive accuracy will be maximized by matching the numerical modified (or scaled) wavenumber with its analytical counterpart [25]. To this end, the Fourier transform $\tilde{u}(\beta)=\frac{1}{2\pi}\int_{-\infty}^{+\infty}u(x)\ e^{-\mathbf{i}\beta x}\ dx$ and its inverse $u(x)=\int_{-\infty}^{+\infty}\tilde{u}(\beta)e^{\mathbf{i}\beta x}\ d\beta$ are performed. Note that the notation $\mathbf{i}$ is equal to $\sqrt{-1}$. We then perform the Fourier transform on each term shown in Eqs. (4.5), (4.6) and (4.7). The effective (or numerical) scaled wavenumber is equated to the actual (or exact) wavenumber β, thereby leading to

$$\begin{aligned}\mathbf{i}\beta' h\ (a_1\exp(-\mathbf{i}\beta h)+1)&=d_1\exp(-\mathbf{i}\beta h)+d_2+d_3\exp(\mathbf{i}\beta h)\\&\quad-(\mathbf{i}\beta'' h)^2(b_1\exp(-\mathbf{i}\beta h)+b_2+b_3\exp(\mathbf{i}\beta h))\\&\quad-(\mathbf{i}\beta''' h)^3(c_1\exp(-\mathbf{i}\beta h)+c_3\exp(\mathbf{i}\beta h)),\end{aligned} \tag{4.16}$$

$$\begin{aligned}\mathbf{i}\beta' h\ \Big(-\frac{29}{16}\exp(-\mathbf{i}\beta h)+\frac{29}{16}\exp(\mathbf{i}\beta h)\Big)&=4\exp(-\mathbf{i}\beta h)-8+4\exp(\mathbf{i}\beta h)\\&\quad-(\mathbf{i}\beta'' h)^2\Big(-\frac{5}{16}\exp(-\mathbf{i}\beta h)+1-\frac{5}{16}\exp(\mathbf{i}\beta h)\Big)\\&\quad-(\mathbf{i}\beta''' h)^3\Big(-\frac{1}{48}\exp(-\mathbf{i}\beta h)+\frac{1}{48}\exp(\mathbf{i}\beta h)\Big),\end{aligned} \tag{4.17}$$

$$\begin{aligned}\mathbf{i}\beta' h\ \Big(-\frac{105}{16}\exp(-\mathbf{i}\beta h)-\frac{105}{16}\exp(\mathbf{i}\beta h)\Big)&=\frac{105}{16}\exp(-\mathbf{i}\beta h)-\frac{105}{16}\exp(\mathbf{i}\beta h)\\&\quad-(\mathbf{i}\beta'' h)^2\Big(-\frac{15}{8}\exp(-\mathbf{i}\beta h)+\frac{15}{8}\exp(\mathbf{i}\beta h)\Big)\\&\quad-(\mathbf{i}\beta''' h)^3\Big(-\frac{3}{16}\exp(-\mathbf{i}\beta h)+1-\frac{3}{16}\exp(\mathbf{i}\beta h)\Big).\end{aligned} \tag{4.18}$$

By solving Eqs. (4.16), (4.17) and (4.18), we can then derive the expression of $\beta' h$.

The numerical scaled wavenumber $\beta' h$ derived above will be used in the analysis of numerical error computed from the proposed combined compact difference scheme. This modified wavenumber is periodic with a period of 2π. In the numerical modified (or scaled) wavenumber $\beta' h$, its real and imaginary parts account respectively for the dispersion error (phase error) and the dissipation error (amplitude error). To get a better dispersive accuracy, we equate βh to $\Re[\beta' h]$, where $\Re[\beta' h]$ denotes the real part of $\beta' h$. This corresponds to demand that the magnitude of the integrated error function $E(\beta)$

defined below in the range $-\frac{\pi}{2}\leq\beta h\leq\frac{\pi}{2}$ should be a very small and positive magnitude

$$E(\beta)=\int_{-\frac{\pi}{2}}^{\frac{\pi}{2}}\left[(\beta h-\Re[\beta' h])\right]^2 d(\beta h). \tag{4.19}$$

To minimize the positive error function defined in $-\frac{\pi}{2}\leq\beta h\leq\frac{\pi}{2}$, the extreme condition is chosen to be $\frac{\partial E}{\partial d_1}=0$. This constraint equation derived from the Fourier analysis is solved together with the other eight algebraic equations derived previously from the modified equation analysis to reduce dissipation error as well as to get an improved dispersion accuracy. The resulting nine introduced unknowns can be uniquely determined as $a_1=1.1875$, $b_1=0.23643236$, $b_2=-0.27774699$, $b_3=-0.01356764$, $c_1=0.01894044$, $c_3=0.00189289$, $d_1=-2.33613227$, $d_2=2.48476453$ and $d_3=-0.14863227$. The above upwinding scheme developed in a stencil of three grid points $i-1$, i and $i+1$ for $\frac{\partial u}{\partial x}$ has the seven spatial order accuracy as the modified equation has the form $\frac{\partial u}{\partial x}=\frac{\partial u}{\partial x}|_{exact}-0.65175737\times10^{-5}\ h^7\frac{\partial^8 u}{\partial x^6}+0.81653294\times10^{-7}\ h^9\frac{\partial^{10}u}{\partial x^{10}}+H.O.T.$ For $u<0$, the non-centered combined compact difference scheme derived similarly in a three-point grid stencil for approximating $\frac{\partial u}{\partial x}$ is

$$\begin{aligned}&\frac{\partial u}{\partial x}\Big|_i+1.1875\frac{\partial u}{\partial x}\Big|_{i+1}+h\left(0.01356764\frac{\partial^2 u}{\partial x^2}\Big|_{i-1}+0.27774699\frac{\partial^2 u}{\partial x^2}\Big|_i-0.23643236\frac{\partial^2 u}{\partial x^2}\Big|_{i+1}\right)\\&\quad+h^2\left(0.00189289\frac{\partial^3 u}{\partial x^3}\Big|_{i-1}+0.01894044\frac{\partial^3 u}{\partial x^3}\Big|_{i+1}\right)\\&=\frac{1}{h}(0.14863227u_{i-1}-2.48476453u_i+2.33613227u_{i+1}).\end{aligned} \tag{4.20}$$

4.3 Discretization of $(u\alpha)_x$

We aim to conserve the flux term $u\alpha$ across a cell of length h. This objective is achieved by means of the approximation $\frac{\partial(u\alpha)}{\partial x}|_i=\frac{u_{i+\frac{1}{2}}\alpha_{i+\frac{1}{2}}-u_{i-\frac{1}{2}}\alpha_{i-\frac{1}{2}}}{h}$. The values of α at the half nodal points $i\pm\frac{1}{2}$ are approximated as

$$\begin{aligned}\alpha_{i+\frac{1}{2}}=d_1^*\alpha_i+d_2^*\alpha_{i+1}-\Bigg[&a_1^*\alpha_{i-\frac{1}{2}}+h\left(b_1^*\frac{\partial\alpha}{\partial x}\Big|_{i-\frac{1}{2}}+b_2^*\frac{\partial\alpha}{\partial x}\Big|_{i+\frac{1}{2}}+b_3^*\frac{\partial\alpha}{\partial x}\Big|_{i+\frac{3}{2}}\right)\\&+h^2\left(c_1^*\frac{\partial\alpha^2}{\partial^2 x}\Big|_{i-\frac{1}{2}}+c_2^*\frac{\partial\alpha^2}{\partial^2 x}\Big|_{i+\frac{3}{2}}\right)\Bigg],\end{aligned} \tag{4.21}$$

and

$$\begin{aligned}\alpha_{i-\frac{1}{2}}=d_1^*\alpha_{i-1}+d_2^*\alpha_i-\Bigg[&a_1^*\alpha_{i-\frac{3}{2}}+h\left(b_1^*\frac{\partial\alpha}{\partial x}\Big|_{i-\frac{3}{2}}+b_2^*\frac{\partial\alpha}{\partial x}\Big|_{i-\frac{1}{2}}+b_3^*\frac{\partial\alpha}{\partial x}\Big|_{i+\frac{1}{2}}\right)\\&+h^2\left(c_1^*\frac{\partial\alpha^2}{\partial x}\Big|_{i-\frac{3}{2}}+c_2^*\frac{\partial\alpha^2}{\partial x}\Big|_{i+\frac{1}{2}}\right)\Bigg].\end{aligned} \tag{4.22}$$

The coefficients a_i^*, b_i^*, c_i^* and d_i^* are then derived by comparing the coefficients derived in Eq. (4.5) for $\frac{\partial\alpha}{\partial x}|_i$. After a term-by-term comparison of the coefficients, the coefficients shown in (4.21) and (4.22) can be derived as $a_1^*=1.1875$, $b_1^*=0.23643236$, $b_2^*=-0.27774699$, $b_3^*=-0.01356764$, $c_1^*=0.01894044$, $c_2^*=0.00189289$, $d_1^*=-2.33613227$ and $d_2^*=-0.14863227$.

4.4 Discretization of P_x and Q_x

The three-point combined compact difference (CCD) scheme derived in [26] to approximate the gradient terms ϕ_x ($\phi=P$ in (3.6) or Q in (3.8)) is given below

$$\frac{h}{16}\frac{\partial^2\phi}{\partial x^2}\Big|_{i-1}-\frac{h}{16}\frac{\partial^2\phi}{\partial x^2}\Big|_{i+1}=\frac{15}{16h}(-\phi_{i-1}+\phi_{i+1})+\left(\frac{7}{16}\frac{\partial\phi}{\partial x}\Big|_{i-1}+\frac{\partial\phi}{\partial x}\Big|_i+\frac{7}{16}\frac{\partial\phi}{\partial x}\Big|_{i+1}\right), \tag{4.23}$$

$$-\frac{1}{8}\frac{\partial^2\phi}{\partial x^2}\Big|_{i-1}+\frac{\partial^2\phi}{\partial x^2}\Big|_i-\frac{1}{8}\frac{\partial^2\phi}{\partial x^2}\Big|_{i+1}=\frac{1}{h^2}(3\phi_{i-1}-6\phi_i+3\phi_{i+1})-\frac{1}{h}\left(-\frac{9}{8}\frac{\partial\phi}{\partial x}\Big|_{i-1}+\frac{9}{8}\frac{\partial\phi}{\partial x}\Big|_{i+1}\right). \tag{4.24}$$

The above center-type CCD scheme developed in a stencil of three grid points $i-1$, i and $i+1$ for $\frac{\partial\phi}{\partial x}$ has sixth-order accuracy.

4.5 Three-point sixth-order accurate Helmholtz scheme

The compact difference scheme developed in [20] for efficiently solving the Helmholtz equation is applied here. A three-point implicit scheme which uses only the adjacent nodes relates u to the partial derivative terms u_{xx} and u_{xxxx}. For the Helmholtz equation (*i.e.* (3.7)), its approximated equation is given below, where $f_i=-(\frac{u_i^2}{2}+\frac{\alpha_i}{2}+2\kappa u_i)$

$$\begin{aligned}&P_{i+1}-\left(2+h^2+\frac{1}{12}h^4+\frac{1}{360}h^6\right)P_i+P_{i-1}\\&=h^2f_i+\frac{1}{12}h^4\left(f_i+\frac{\partial^2 f_i}{\partial x^2}\right)+\frac{1}{360}h^6\left(f_i+\frac{\partial^2 f_i}{\partial x^2}+\frac{\partial^4 f_i}{\partial x^4}\right).\end{aligned} \tag{4.25}$$

Application of the above three-point compact difference scheme for Eq. (3.7) indeed yields sixth-order accuracy in space because the corresponding modified equation can be derived as $\frac{\partial^2 P}{\partial x^2}-P=f+\frac{h^6}{20160}\frac{\partial^8 P}{\partial x^8}+\frac{h^8}{1814400}\frac{\partial^{10}P}{\partial x^{10}}+\cdots+H.O.T.$.

4.6 Solution algorithm

To get the solution u^{n+1} from u^n we adopt the iterative solution algorithm because the value of P which involves the value of $\alpha(\equiv u^2+(u_x)^2)$ and u is required to solve Eq. (3.6). For the sake of clearness, the iterative solution algorithm is summarized as follows:

Step 1: Start from the initial guess for $u^{[\bar{k}],(i)}$ for $i=1,2,3$. Note that $\bar{k}$ denotes the iteration counter.

Step 2: Solve the Eq. (3.8) to get $\alpha^{[\bar{k}],(i)}$ for $i=1,2,3$.
Step 3: The Helmholtz equation (3.7) is solved to get $P^{[\bar{k}],(i)}$ for $i=1,2,3$ by the proposed three-point sixth-order accurate compact Helmholtz scheme described in Section 4.5.
Step 4: Discretize $u_x^{[\bar{k}],(i)}$ and $P_x^{[\bar{k}],(i)}$ by the scheme given in Section 4.2 and Section 4.4 so as to get $F(\equiv -P_x - uu_x)^{[\bar{k}],(i)}$, $i=1,2,3$.
Step 5: Based on the applied symplectic Runge-Kutta method presented in Section 4.1 for (3.6), Eqs. (4.1)-(4.3) are solved simultaneously (or implicitly) for getting the values of $u^{[\bar{k}+1],(i)}$, $i=1,2,3$.
Step 6: Repeat the calculation from **Step 2** to **Step 5** until the residuals, cast in the maximum norms, of Eqs. (4.1)-(4.3) satisfy the convergence criterion $\mathbf{Max}_{x_{j,j=1,N}}(|u^{[\bar{k}+1],(i)} - u^{[\bar{k}],(i)}|, |\alpha^{[\bar{k}+1],(i)} - \alpha^{[\bar{k}],(i)}|) \leq 10^{-9}$, where N denotes the number of grid points.
Step 7: Use Eq. (4.4) to update u^{n+1}.

5 Fundamental analysis of the proposed scheme and verification studies

5.1 Fundamental analysis of the proposed scheme

The solution for the model equation $u_t + c\ u_x = 0$ can be represented by $u = \hat{u}_\beta(t)e^{\mathbf{i}\alpha x}$, where $\mathbf{i} \equiv \sqrt{-1}$ and $\hat{u}_\beta$ is the Fourier mode of the wave number β. Differentiation of the above equation leads to $\frac{\partial u}{\partial x}|_{exact} = \mathbf{i}\beta h \frac{\hat{u}_\beta}{h} e^{\mathbf{i}\beta x}$. Note that the wavenumber has been scaled by $h = \frac{L}{N}$, where L and N denote the length of physical domain and the number of grid intervals, respectively. The approximated derivative term $\frac{\partial u}{\partial x}$ can be similarly written as

$$\left.\frac{\partial u}{\partial x}\right|_{numerical} = \mathbf{i}\beta' h \frac{\hat{u}_\beta}{h} e^{\mathbf{i}\beta x} = (K_r + \mathbf{i}K_i)\frac{\hat{u}_\beta}{h} e^{\mathbf{i}\beta x}. \tag{5.1}$$

In the above, K_r and K_i denote the real and imaginary parts, respectively. In other words, two coefficients K_i and K_r accounting respectively for the dispersion and dissipation errors are expressed in terms of the real part $(\beta' h)$ and the imaginary part $(\beta' h)$ as $K_i = \Re[\beta' h]$ and $K_r = -\Im[\beta' h]$.

In Fig. 1, the values of K_i and K_r are plotted with respect to the scaled wavenumber αh using the three-point upwinding combined compact difference scheme CCD derived in Section 4.2. One can conclude from the two plots in this figure that the proposed upwind scheme performs better than the other scheme [24] because of the improved dispersive accuracy. The positive-valued K_r calculated from the present CCD scheme is found to be less accurate than the non-dissipative (or $K_r = 0$) center-type combined compact difference scheme of Nihei and Ishii [24].

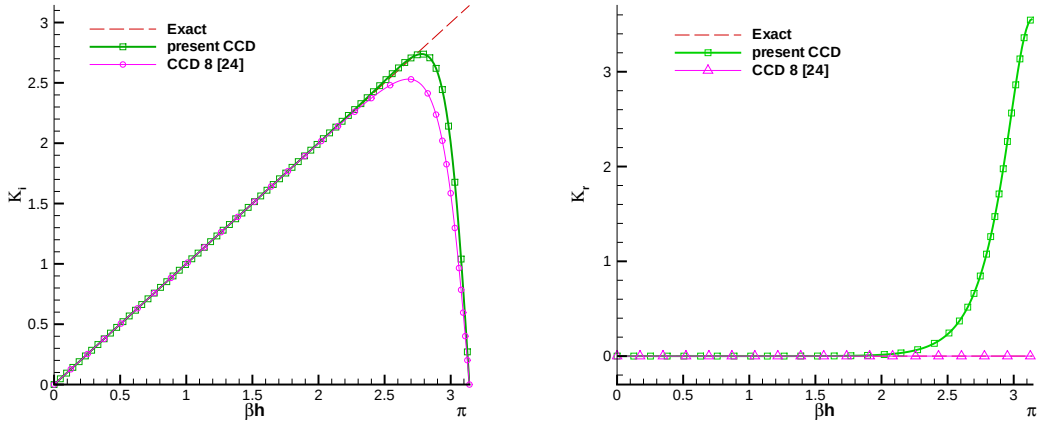

(a) (b)

Figure 1: Comparison of the plots for $K_r(\alpha h)$ and $K_i(\alpha h)$ between the proposed three-point seventh-order accurate upwinding combined compact difference scheme (CCD) and the three-point eighth-order accurate centered combined compact difference scheme (CCD8) [24]. (a) K_i; (b) K_r.

5.2 Verification studies

The analytic problem admitting a periodic travelling wave solution $u(x,t)=U(x-ct)$ is chosen to justify the integrity of the developed scheme for solving the nonlinear CH equation [20].

$$U'=\pm\sqrt{\frac{-U^3+(c-2\kappa)U^2+C(A)U}{c-U}} \tag{5.2}$$

Note that A and U are implicitly related to the independent variable x by

$$x=\frac{2}{\sqrt{a_1(a_2-a_3)}}(a_1-a_2)\Pi, \tag{5.3}$$

where Π is the elliptic function,

$$a_1=c,\quad a_2=\frac{1}{2}\left(c-2\kappa+\sqrt{(c-2\kappa)^2+4C}\right),\quad a_3=\frac{1}{2}\left(c-2\kappa-\sqrt{(c-2\kappa)^2+4C}\right). \tag{5.4}$$

Calculation will be carried out at $c=2$, $\kappa=1/2$ and $C=1$ in this validation study. The spatial rates of convergence is approximately equal to 5.25 computed from the L_2 error norms. The spatial rates of convergence has been shown in Table 1. Note that the time step $\Delta t=\frac{6.3019}{128}\times10^{-5}$ is much smaller than the grid size Δx.

Table 1: The predicted spatial rates of convergence for the test problem given in Section 5.2.

Grids	32	64	128
L_2-error norm	6.1005E-4	9.7343E-6	4.1842E-7
rate of convergence	—	5.9697	4.54002

6 Numerical results

To make an indirect verification of the predicted CH solution, in this section the following Hamiltonians are computed and are plotted with respect to time for all the test problems

$$H_0 = \int u\,dx, \tag{6.1}$$

$$H_1 = \frac{1}{2}\int (u^2+u_x^2)\,dx = \int \alpha\,dx, \tag{6.2}$$

$$H_2 = \frac{1}{2}\int (u^3+uu_x^2+2\kappa u^2)\,dx = \int u\,\alpha\,dx, \tag{6.3}$$

$$\begin{aligned} H_3 &= \int (u^2+\frac{1}{2}u_x^2)P+\frac{u^2}{4}(u^2+2u_x^2)\,dx \\ &= \frac{1}{2}\int (\alpha+u^2)P+\frac{u^2}{2}(2\alpha-u^2)\,dx, \end{aligned} \tag{6.4}$$

$$M = \int (u-u_{xx})\,dx. \tag{6.5}$$

6.1 CH solutions obtained at $\kappa = 0$

6.1.1 Peakon-peakon problem

The problem with two peakons propagating along the same direction will be solved at $\kappa = 0$ in the domain $-60 \le x \le 60$. The solution will be sought subject to the following initial data for the CH equation (2.1)

$$u_0(x,t=-20) = p_1(t)e^{-|x-q_1(t)|}+p_2(t)e^{-|x-q_2(t)|}. \tag{6.6}$$

Two investigated peakons move rightwards with $p_1(t) = \frac{c_2E_1+c_1E_2}{E_1+E_2}$ and $p_2(t) = \frac{c_1E_1+c_2E_2}{E_1+E_2}$, where $E_i(t) = e^{c_it}$ $(i = 1,2)$, $c_1 = 1.6$ and $c_2 = 1.0$. The Camassa-Holm equation will be solved subject to the specified periodic boundary conditions at $q_1(t) = \ln[\frac{(c_1-c_2)E_1E_2}{c_2E_1+c_1E_2}]$ and $q_2(t) = \ln[\frac{c_1E_1+c_2E_2}{c_1-c_2}]$.

In Fig. 2, the predicted time-evolving two-peakon solutions in a domain of 1024 uniformly discretized grids compare excellently with the exact solutions given in [27]. Two peakons pass through each other and both of them remain as the solitary waves. The switching scenario is therefore clearly exhibited in this peakon-peakon problem. Since wave breaking has not been observed, this problem permits a global solution. The higher

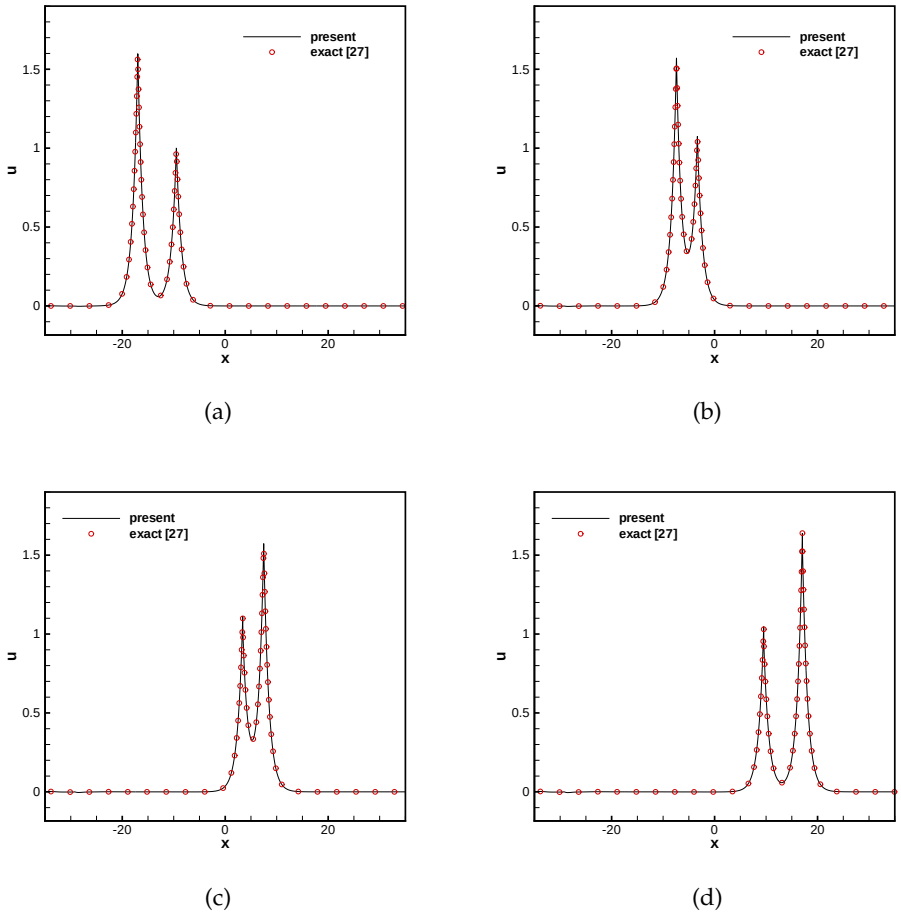

Figure 2: Comparison of the predicted and exact peakon-peakon CH solutions computed at different times in a domain of 1024 grids. (a) $t=-10.0$; (b) $t=-2.0$; (c) $t=2.0$; (d) $t=10.0$.

peakon is observed to propagate faster than the lower peakon. At $t=0^+$, the higher peakon has already overtaken the lower peakon. While there exists an exchange of $\int u\,dx$ between the two moving peakons, the Hamiltonians shown in Fig. 3 are unchanged at all times. In addition, the applied $u-P-\alpha$ formulation is validated in view of the predicted L_2-error norms and the spatial rates of convergence shown in Table 2.

Table 2: The predicted L_2-error norms at $t=-19$ for the calculations obtained in $-60\leq x\leq -33$ and at $\Delta t=3\times 10^{-6}$ using three different mesh sizes. This problem is described in Section 6.1.1.

Grids	512	1024	2048
L_2-error norm	2.7020E-2	1.0223E-3	8.9161E-5
rate of convergence	—	4.721	3.51925

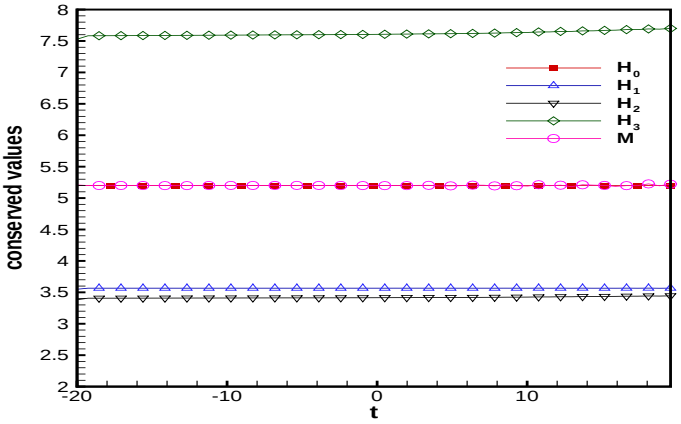

Figure 3: The computed values of the Hamiltonians H_0, H_1, H_2, H_3 and M are plotted with respect to time for the investigated peakon-peakon problem in Section 6.1.1.

6.1.2 Peakon-antipeakon problems

The Camassa-Holm equation admits peakon solution [28]. Peakon (or peaked solitary wave) is a soliton having a finite-valued discontinuous first derivative. Peakon solution can be algebraically expressed by $u(x,t)=ce^{-|x-ct|}$. For $c<0$, the wave propagates leftwards with its peak pointing downward. Such a peaked soliton is called as an antipeakon.

One-peakon and one-antipeakon problem

The peakon and antipeakon initial condition given below is considered in this subsection

$$u(x,t=0)=e^{-|x+5|}-e^{-|x-5|}. \tag{6.7}$$

The wave speed c and the collision time t_c can be obtained as $c\simeq 0.999977299777468$ and $t_c\simeq 5.693265068768256$ by solving the equations $\ln[\text{sech}(-c\ t_c)]=-5$ and $\frac{c}{\tanh(-c\ t_c)}=-1$ [29]. Following the notations given in [29], the solution of Eq. (2.1) for the peakon/antipeakon collision problem can be expressed as [29]

$$u(x,t)=\frac{c}{\tanh(c(t-t_c))}[e^{-|x-q(t)/2|}-e^{-|x+q(t)/2|}], \tag{6.8}$$

where $q(t)=-\ln[\text{sech}^2(t-t_c)]$. The number of cells used in this simulation study is 2048 in the domain [-25, 25]. The time step is $\Delta t=0.01\Delta x$. Fig. 4 shows the solution computed from the proposed scheme and the exact solution of Eq. (6.8). Both of the wave speed and the collision time are well predicted even near the point of collision. Fig. 5 shows that all the Hamiltonians shown in (6.1)-(6.5) remain unchanged before and after the collision time, thereby illustrating that at a time after peakon/antipeakon collision the peakon and antipeakon pass through each other without changing the Hamiltonian values.

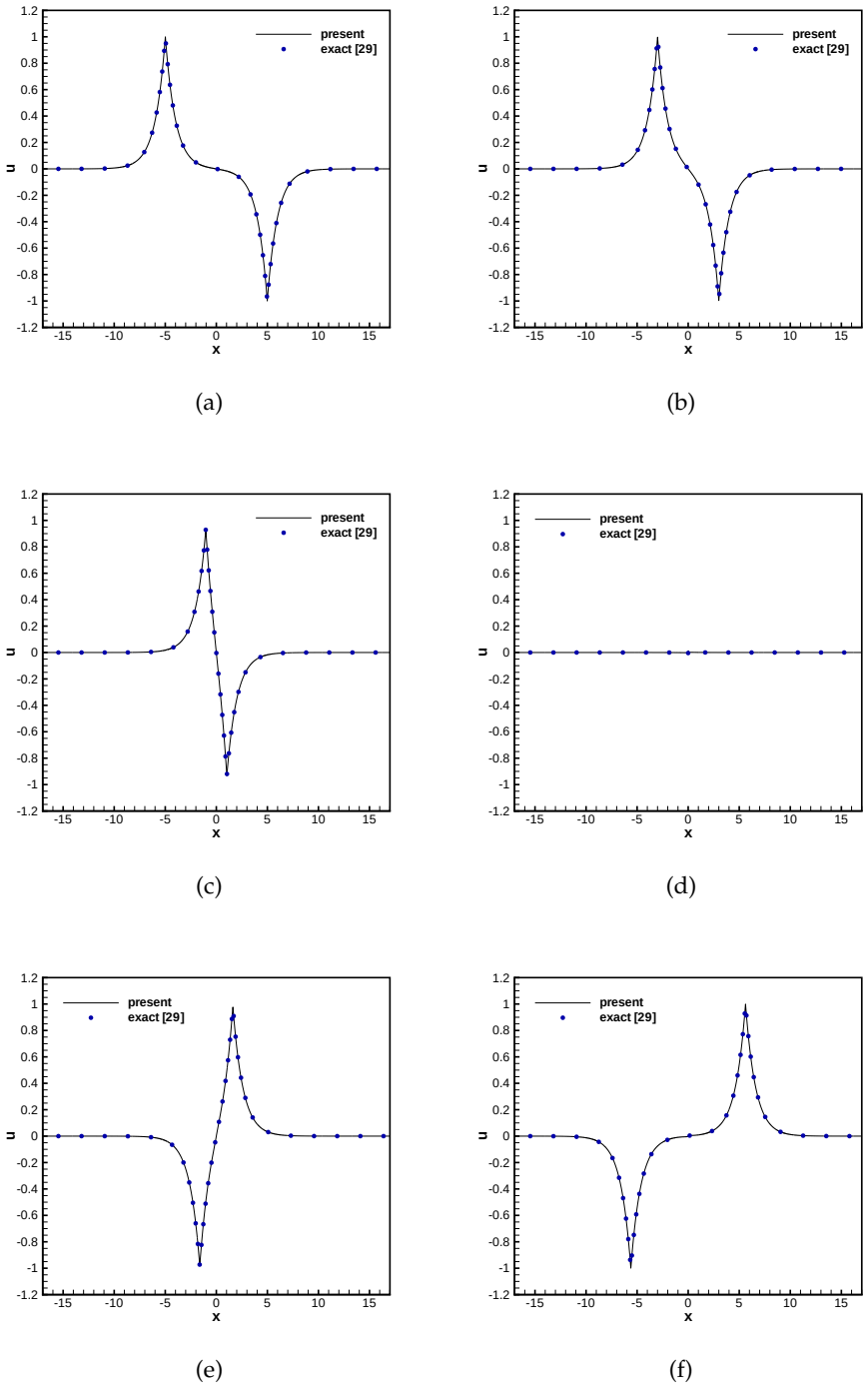

Figure 4: Comparison of the predicted and exact peakon-antipeakon CH solutions computed in the domain of 2048 grids at different times. (a) $t=0.0$; (b) $t=2.0$; (c) $t=4.0$; (d) $t_c=5.693265068768256$; (e) $t=8.0$; (f) $t=12.0$.

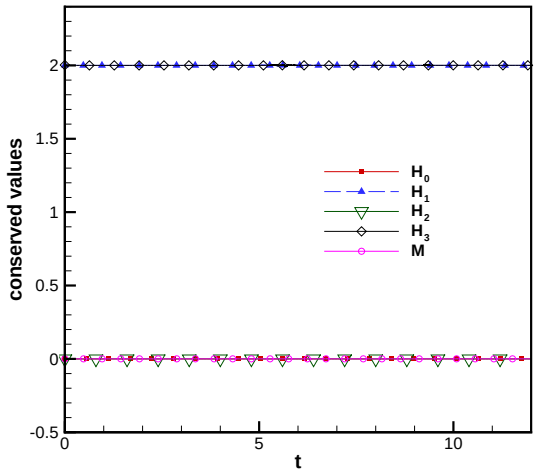

Figure 5: The computed values of the Hamiltonians H_0, H_1, H_2, H_3 and M are plotted with respect to time for the investigated one-peakon and one-antipeakon problem.

Two-peakon and one-antipeakon problem

Eq. (2.1) subject to the periodic boundary condition and the initial condition given below is then solved in $0 \leq x \leq 80$

$$u(x,t=0) = 3e^{-|x-10|} + e^{-|x-50|} - 2e^{-|x-65|}. \tag{6.9}$$

This initial solution profile is the combination of peakon-peakon and peakon-antipeakon profiles. Based on the solutions plotted in Fig. 6 in the domain of 2048 nodal points, the computed Hamiltonians are plotted versus time in Fig. 7. The unchanged values of Hamiltonians in time exhibit again the non-dissipative interaction mechanism after a time of the collision of two peakons and one antipeakon.

Three-peakon and one-antipeakon problem

The three-peakon and one-antipeakon case was studied previously by Holden and Raynaud [30]. In the domain $-20 \leq x \leq 20$, the following initial condition for the calculation of CH equation is considered

$$u(x,t=0) = p_1(t)e^{-|x-q_1(t)|} + p_2(t)e^{-|x-q_2(t)|} + p_3(t)e^{-|x-q_3(t)|} + p_4(t)e^{-|x-q_4(t)|}. \tag{6.10}$$

In the above, $(q_1,q_2,q_3,q_4) = (-10,-5,0,5)$. Subject to the periodic boundary condition, Eq. (2.1) will be solved at $p_1 = 5$, $p_2 = 5$, $p_3 = 5$ and $p_4 = -12$. The predicted solutions for the three right-running peakons and the single left-running antipeakon in the domains of 2048 and 8192 nodal points are plotted in Fig. 8. We plot the values of H_1 and H_2 with respect to time in Fig. 9 to exhibit the existence of a globally non-dissipative multipeakon-antipeakon solution, which has the nature in contrast to the dissipative scenario wrongly predicted earlier by Sheu et al. in [20] using the $u-P$ formulation.

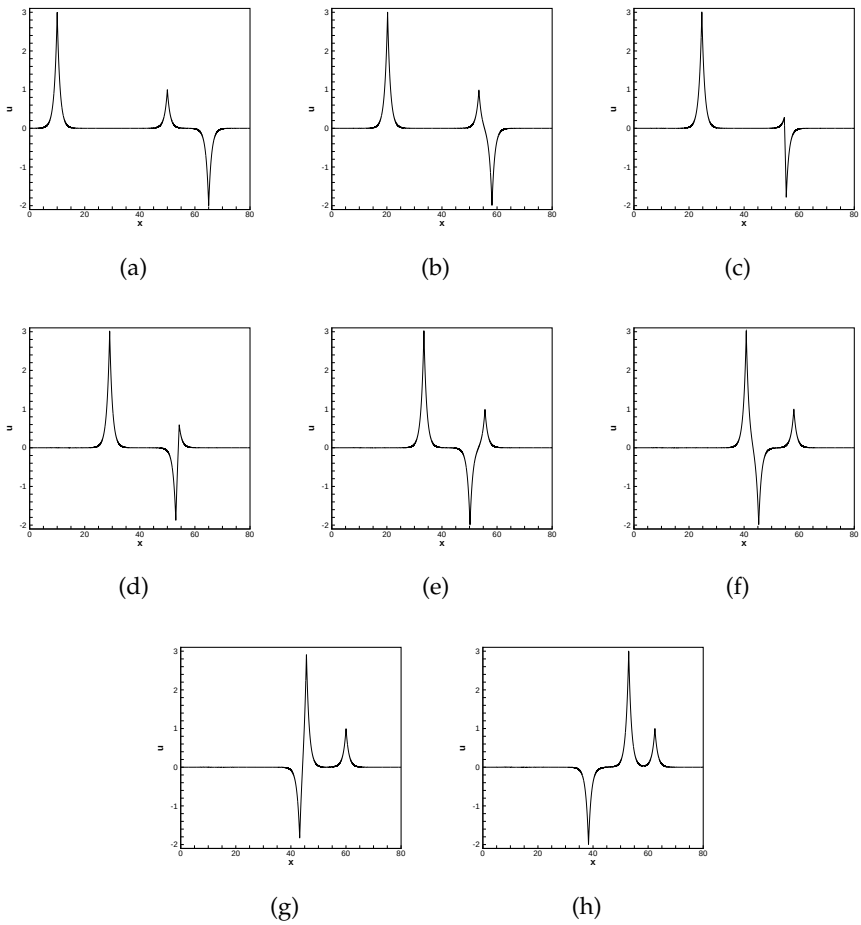

Figure 6: The CH solutions computed in a domain of 2048 grids at different times. (a) $t=0.0$; (b) $t=3.514$; (c) $t=5.02$; (d) $t=6.526$; (e) $t=8.032$; (e) $t=10.542$; (e) $t=12.55$; (f) $t=15.06$.

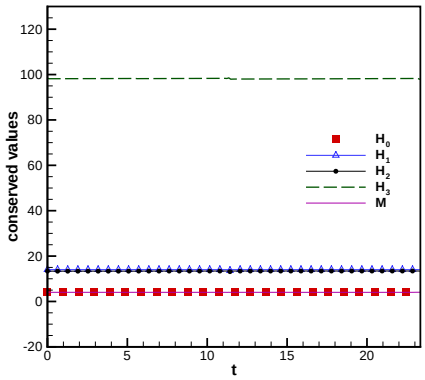

Figure 7: The computed Hamiltonians H_0, H_1, H_2, H_3 and M are plotted with respect to time for the investigated two-peakon plus one-antipeakon problem.

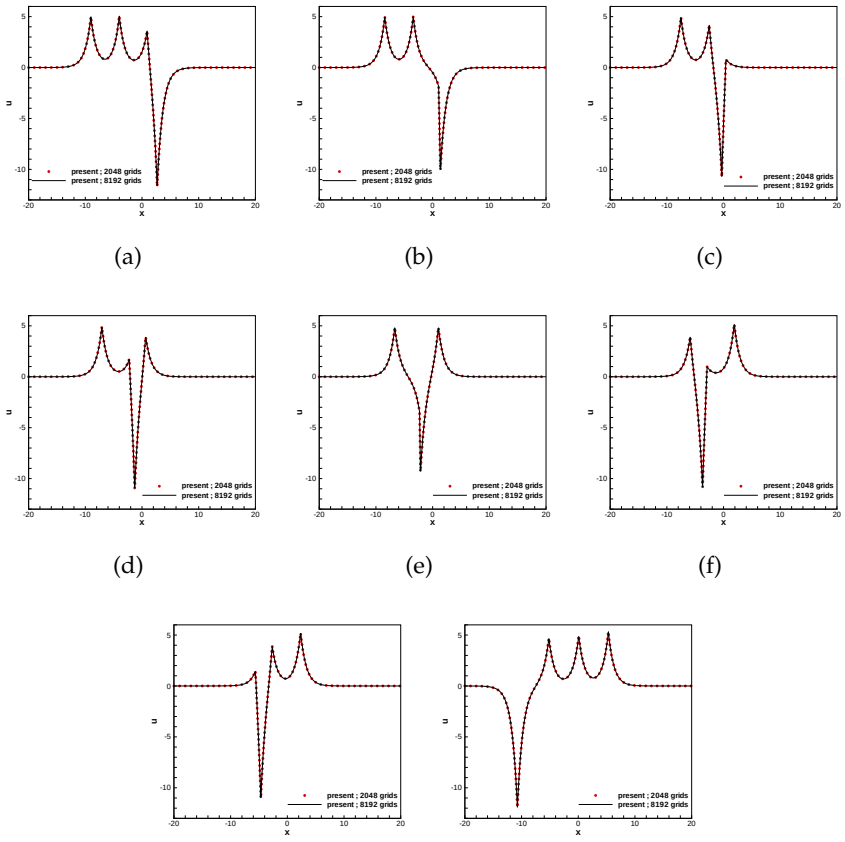

(a) (b) (c)

(d) (e) (f)

(g) (h)

Figure 8: The predicted CH solutions computed in the domains of 2048 and 8192 grids at different times. (a) t=0.1953; (b) t=0.3125; (c) t=0.4980; (d) t=0.5860; (e) t=0.6690; (f) t=0.8398; (g) t=0.9277; (h) t=1.8493.

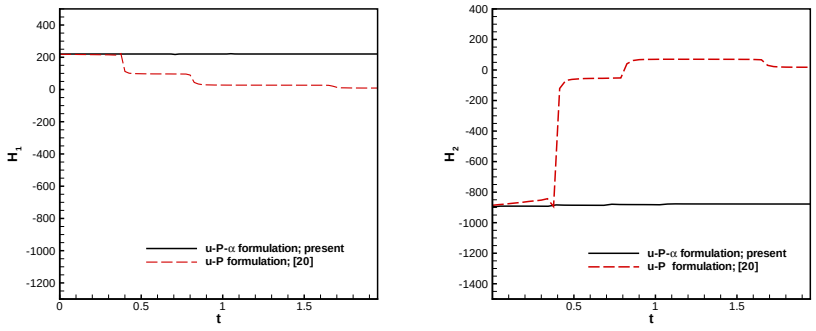

(a) (b)

Figure 9: The computed Hamiltonians H_1 and H_2 are plotted with respect to time for the investigated three-peakon plus one-antipeakon problem. (a) H_1; (b) H_2.

6.2 CH solutions obtained at $\kappa \neq 0$

6.2.1 One soliton problem

We now consider the example of one soliton case with the solution profile given by [8]:

$$u(y,t) = \frac{2p^2cv}{(c^2+p^2)+(c^2-p^2)\cosh\xi}, \quad x = 2cy + \ln\left(\frac{g}{h}\right). \tag{6.11}$$

In the above, $g = 1+(\frac{c-p}{c+p})e^{\xi}$, $h = 1+(\frac{c+p}{c-p})e^{\xi}$, $\xi = p(2y-vt)$, $v = \frac{2}{c^2-p^2}$ with $c = \frac{1}{\kappa} = 10.0$ and $p = 9.12$. The time-evolving solution plotted in Fig. 10 compares well with the exact solution given in [8]. As before, the computed Hamiltonians are plotted against time in

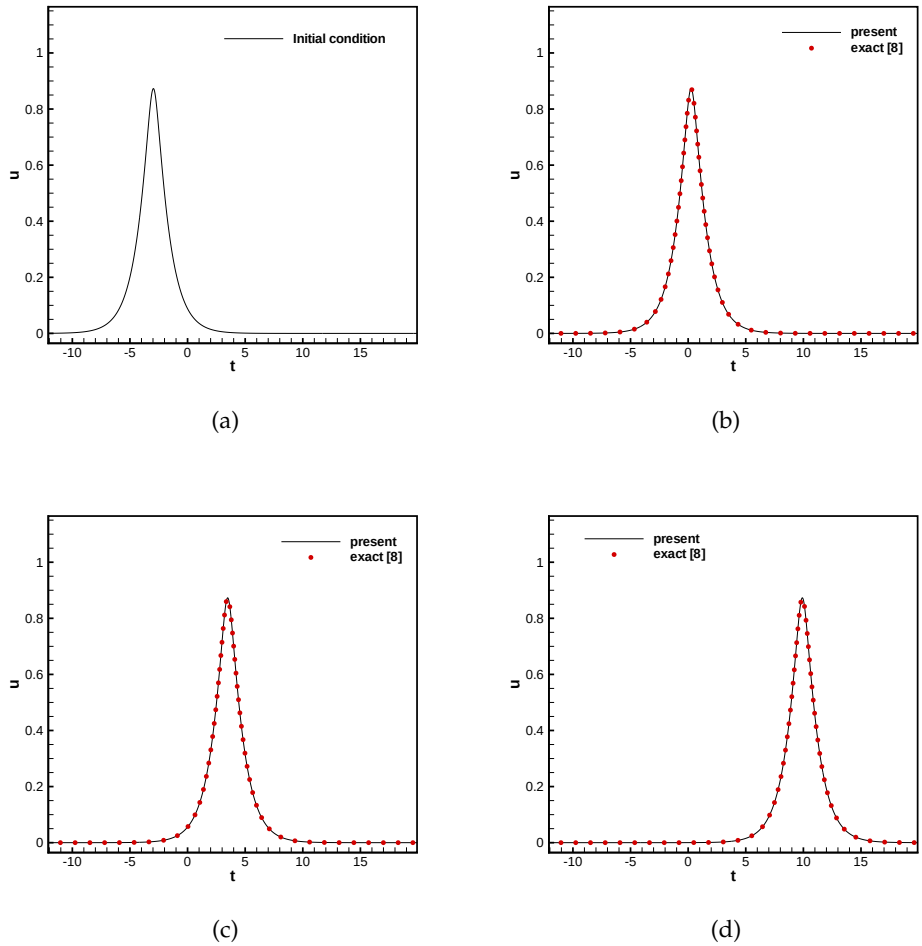

Figure 10: Comparison of the CH solutions, computed in a domain of 1024 grids, with the exact solutions at different times. (a) $t = 0.0$; (b) $t = 3.0$; (c) $t = 6.0$; (d) $t = 12.0$.

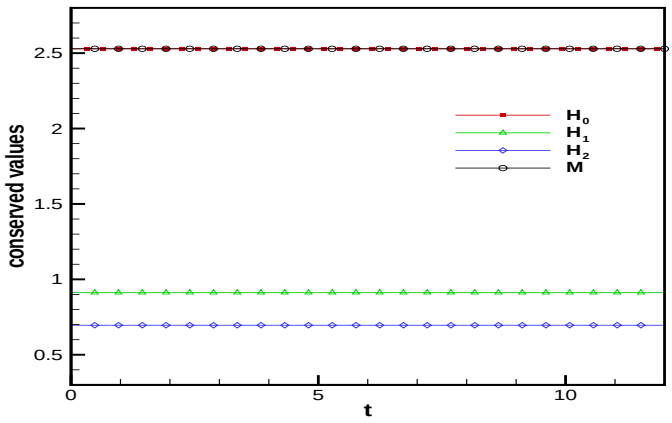

Figure 11: The predicted values of the Hamiltonians H_0, H_1, H_2 and M are plotted with respect to time for the investigated soliton problem in Section 6.2.1.

a domain of 1024 nodal points. One can clearly see from Fig. 11 that all the predicted Hamiltonians remain almost unchanged. The proposed CH scheme is verified under the condition of nonzero k.

6.2.2 One cuspon problem

Cuspon also involves the discontinuous first derivative. In contrast to the peakon solution, the slopes of cuspon solution are infinitely large at the locations immediately adjacent to the point having the discontinuous first derivative [32]. The one cuspon solution is given by

$$u(y,t)=\frac{2p^2cv}{(c^2+p^2)-(c^2-p^2)\cosh\xi},\quad x=2cy+\ln\left(\frac{g}{h}\right). \tag{6.12}$$

In the above, $g=1-(\frac{c-p}{c+p})e^{\xi}$, $h=1-(\frac{c+p}{c-p})e^{\xi}$, $\xi=p(2y-vt)$, $v=\frac{2}{c^2-p^2}$ with $c=\frac{1}{\kappa}=10.0$ and $p=10.15$ [8].

Approximation of the convective terms shown in Eq. (3.6) needs to take the upwinding nodal solutions along the flow direction into a favorable consideration. In Section 4.2, an upwinding combined compact difference scheme having a better dispersion relation has been developed to solve the first derivative term in (3.6). Our primary aim is to enhance convective stability of the Eq. (3.6) by virtue of the increased dispersive accuracy. We also compare the numerical result which uses the weighted essentially non-oscillatory scheme [31] to solve the convective terms in (3.6).

The time-evolving one-cuspon solution was predicted in a mesh of 4096 uniformly discretized grids. Fig. 12 shows the results computed at the three chosen times. For the sake of verification, we also plot in Fig. 13 the values of $H_0\sim H_2$ and M, which are all shown to be unchanged with time, for the case investigated at $\kappa=0.1$.

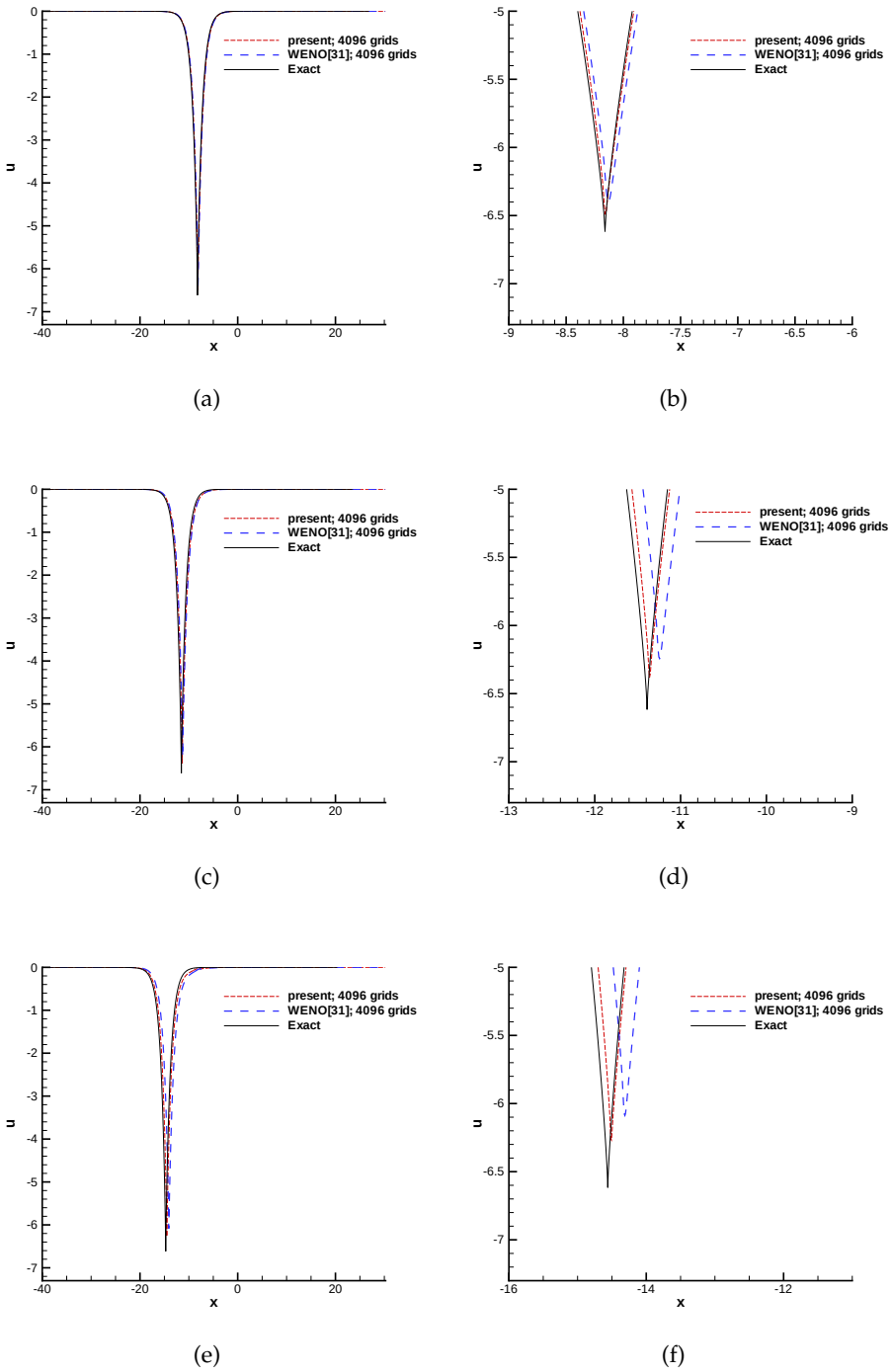

Figure 12: The anticuspon solutions computed in a domain of 4096 grids at different times. (a),(b) $t=0.5$; (c),(d) $t=1.0$; (e),(f) $t=1.5$.

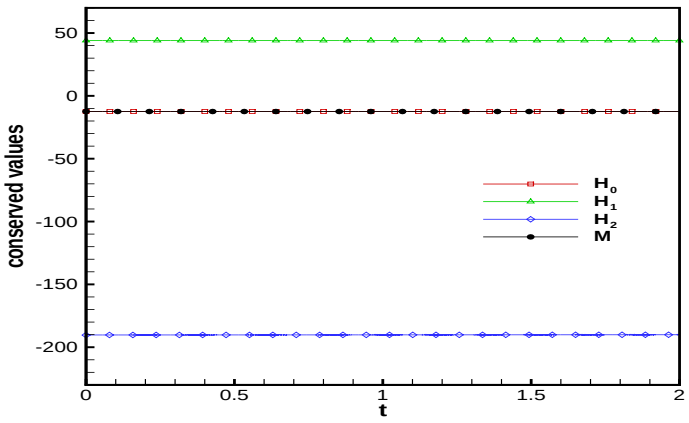

Figure 13: The predicted values of the Hamiltonians H_0, H_1, H_2 and M are plotted with respect to time for the investigated problem in Section 6.2.2.

6.2.3 Soliton-soliton problem

Based on the $u-P-\alpha$ formulation, Eq. (2.1) is solved at $\kappa=(0.24)^2$ for the soliton-soliton case considered previously in [27]. The results computed in a domain of 1024 uniform mesh points will be compared with the results computed by the method of PQ-decomposition in [27].

Fig. 14(a) shows the initial condition ($t=-6.0$), and Figs. 14(b)-14(d) display the time-evolving collision of solitons at three different times. As shown in Fig. 14, after collision the two-soliton solution regains its shape without showing any phase shift. For the sake of verification, the computed values of the Hamiltonians are plotted with respect to time in Fig. 15.

6.2.4 Cuspon-cuspon problem

The equations for getting the cuspon-cuspon solution are as follows

$$u(y,t)=\left(\ln\frac{g}{h}\right)_t, \quad x=2cy+\ln\left(\frac{g}{h}\right). \tag{6.13}$$

In the above equations, g and h can be expressed below as the functions of $\xi_1=p_1(2y-v_1t-8.0)$, $\xi_2=p_2(2y-v_2t-9.0)$, $v_1=\frac{2}{c^2-p_1^2}$ and $v_2=\frac{2}{c^2-p_2^2}$ [8]

$$g=1+\left|\frac{c-p_1}{c+p_1}\right|e^{\xi_1}+\left|\frac{c-p_2}{c+p_2}\right|e^{\xi_2}+\left|\frac{(c-p_1)(c-p_2)}{(c+p_1)(c+p_2)}\right|\left(\frac{p_1-p_2}{p_1+p_2}\right)^2e^{\xi_1+\xi_2}, \tag{6.14}$$

$$h=1+\left|\frac{c+p_1}{c-p_1}\right|e^{\xi_1}+\left|\frac{c+p_2}{c-p_2}\right|e^{\xi_2}+\left|\frac{(c+p_1)(c+p_2)}{(c-p_1)(c-p_2)}\right|\left(\frac{p_1-p_2}{p_1+p_2}\right)^2e^{\xi_1+\xi_2}. \tag{6.15}$$

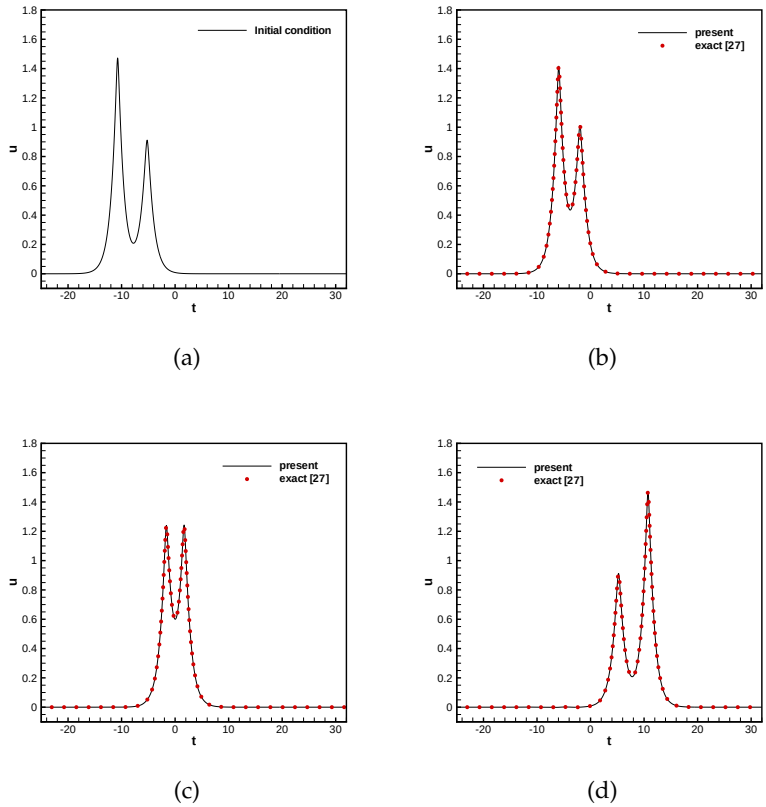

Figure 14: Comparison of the predicted and exact soliton-soliton solutions in a domain of 1024 grids at different times. (a) $t=-6.0$; (b) $t=-3.0$; (c) $t=0.0$; (d) $t=6.0$.

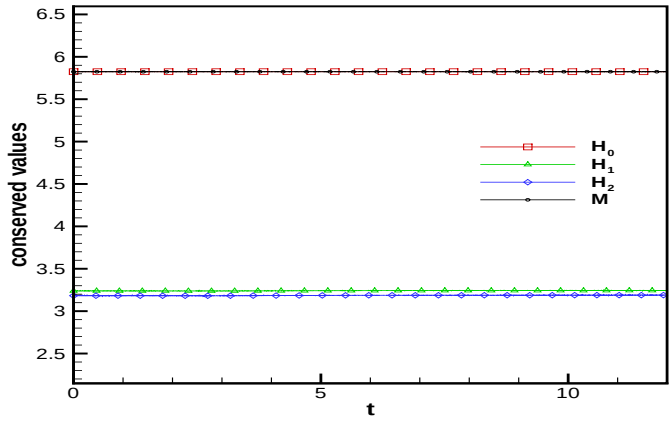

Figure 15: The predicted values of the Hamiltonians H_0, H_1, H_2 and M are plotted with respect to time for the investigated soliton-soliton problem in Section 6.2.3.

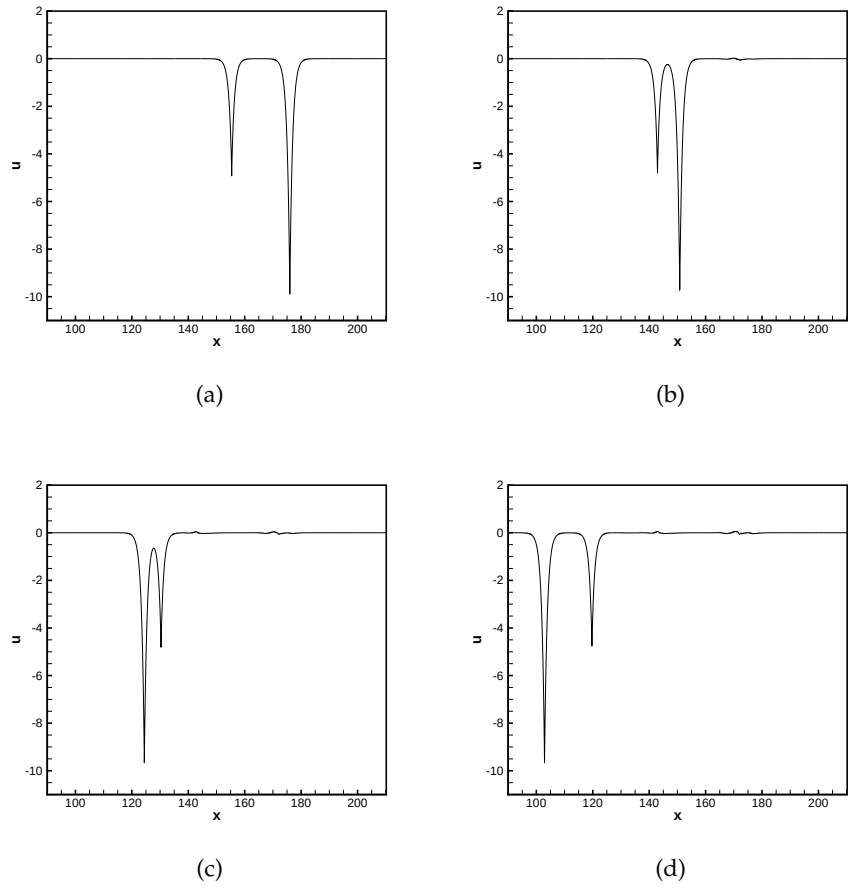

Figure 16: The predicted CH solutions in a domain of 4096 grids at different times. (a) $t=0.0$; (b) $t=2.5714$; (c) $t=5.1428$; (d) $t=7.3469$.

Note that the above expressions include the soliton-soliton solution ($p_1<c, p_2<c$), the cuspon-cuspon solution ($p_1>c, p_2>c$), and the soliton-anticuspon solution ($p_1<c, p_2>c$) [8]. For the cuspon-cuspon case, we chose $p_1=10.2$, $p_2=10.1$ and $c=\frac{1}{\kappa}=10.0$ in this study.

Given the initial solution plotted in Fig. 16(a), the solutions predicted at several different times are illustrated in Figs. 16(b)-(d). As mentioned in [8], two cuspon points always show their presence during the collision. One can clearly see from Fig. 17 that the predicted Hamiltonians remain almost unchanged. The proposed CH scheme is validated again.

6.2.5 Soliton-anticuspon problem

As for the soliton-anticuspon interaction problem, it is defined by $u(y,t)=(\ln\frac{g}{h})_t$, with $\xi_1=p_1(2y-v_1t-2.0)$, $\xi_2=p_2(2y-v_2t-3.0)$, $v_1=\frac{2}{c^2-p_1^2}$, $v_2=\frac{2}{c^2-p_2^2}$ [8]. In Fig. 18(a), we

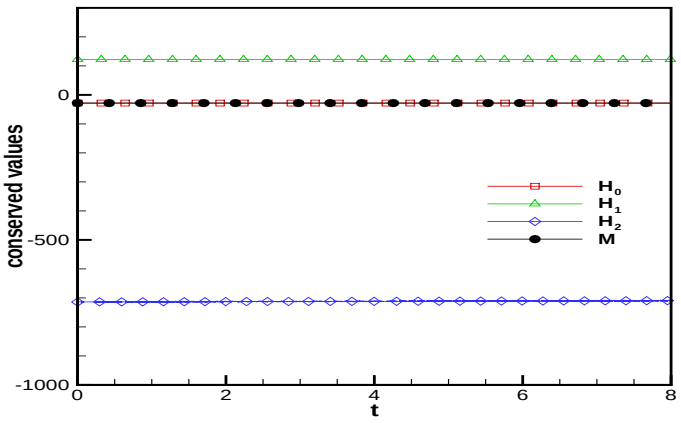

Figure 17: The predicted values of the Hamiltonians H_0, H_1, H_2 and M are plotted with respect to time for the investigated cuspon-cuspon problem in Section 6.2.4.

plot the initial soliton ($p_1=9.8$) and the anticuspon ($p_2=10.1$) at $c=\frac{1}{\kappa}=10.0$. One soliton initially proceeds to the right and the other anticuspon moves to the left. The computed time-evolving solutions plotted in Figs. 18 (b)-(f) compare very well with the exact results given in [8]. One can find from these predicted solutions that soliton disappears after the collision time at $t_c=1.5429$. The total annihilation scenario is, thus, exhibited even at a time of head-on collision. The computed values of all Hamiltonians are also plotted with respect to time in Fig. 19.

7 Concluding remarks

The Camassa-Holm equation is solved by the $u-P-\alpha$ formulation which alleviates the need to approximate the space-time mixed derivative and high-order dispersive terms, thereby considerably simplifying the computation. Moreover, some existing schemes developed for hydrodynamic equations can be applied. We approximate the time derivative term in a three-point grid stencil by the sixth-order accurate implicit symplectic Runge-Kutta scheme so that the conserved properties in the Camassa-Holm equation can be perfectly retained in the discrete context. As for the first-order spatial derivative terms shown in the $u-P-\alpha$ equations, the dispersion error predicted from the proposed seventh-order accurate upwind combined compact difference scheme is minimized. For the peakon-peakon, soliton-soliton and cuspon-cuspon interaction problems, our simulation results clearly exhibit exchange of mass between two waves propagating along the same direction without exhibiting wave breaking. While mass exchange between the individual peakons of different heights is found, the total mass and Hamiltonians remain unchanged when the higher peakon, which propagates faster than the lower one, overtakes the slower-moving peakon. As a result, for the non-collision problems

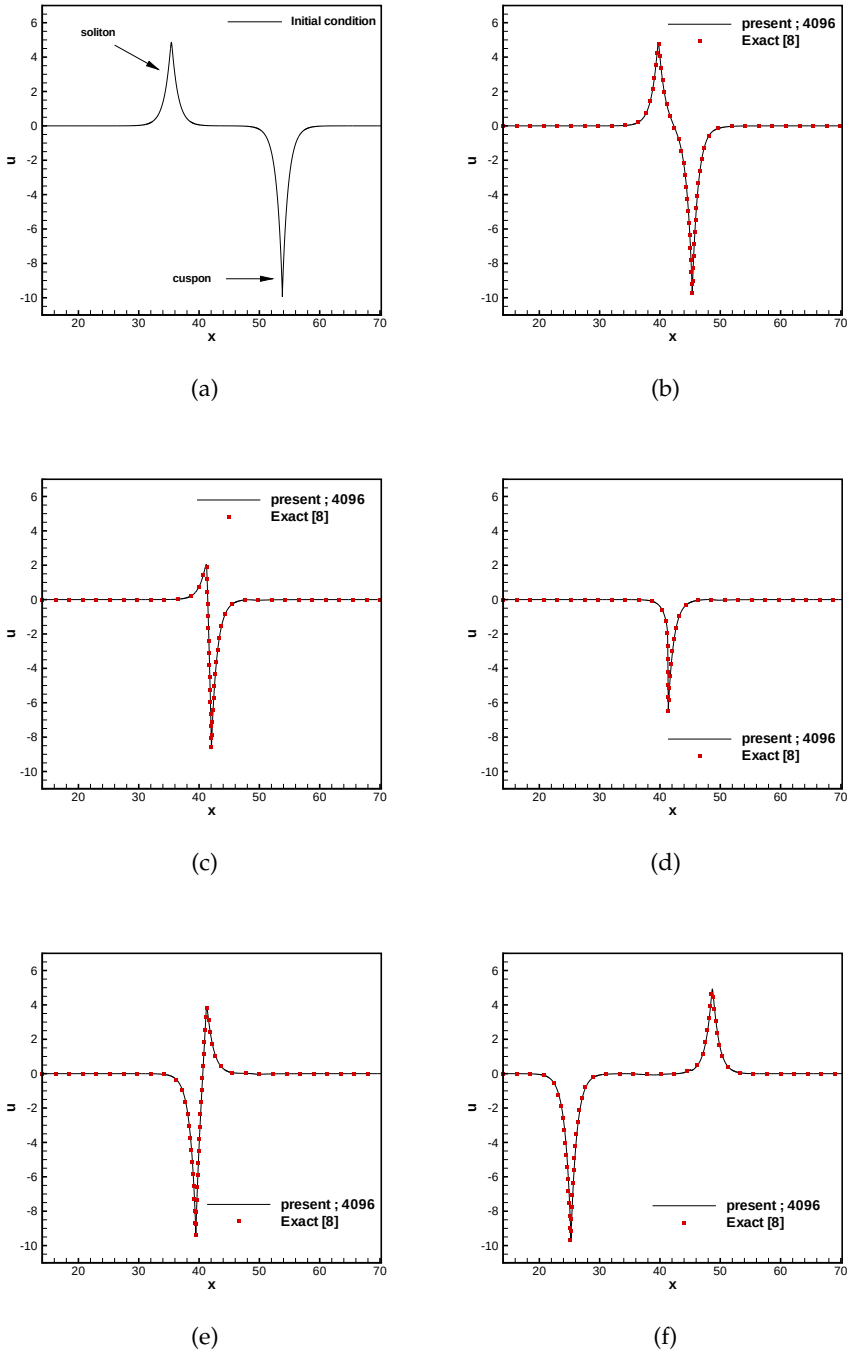

Figure 18: Comparison of the predicted and exact soliton-anticuspon solutions in a domain of 4096 grids at different times. (a) $t=0.0$; (b) $t=0.8574$; (c) $t=1.2$; (d) $t=1.2857$; (e) $t=1.5429$; (f) $t=3.0$.

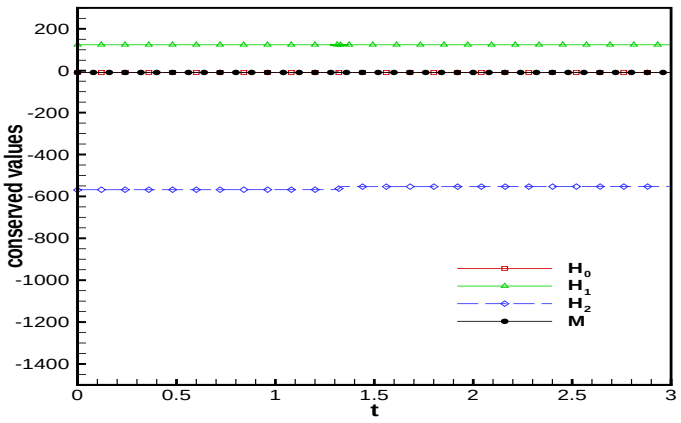

Figure 19: The predicted values of the Hamiltonians H_0, H_1, H_2 and M are plotted with respect to time for the investigated soliton-anticuspon problem in Section 6.2.5.

the switching scenario is numerically confirmed to exist in the Camassa-Holm equation. Also, for the peakon-antipeakon and soliton-anticuspon problems, all the Hamiltonians remain unchanged as well even after the collision. The Camassa-Holm equation permitting non-dissipative (or elastic) collision nature of the solution is therefore numerically demonstrated.

Acknowledgments

This research is supported by National Science Council through the Grants NSC 98-2628-M-002-006, 98-2811-E-002-006 and Fundamental Research Funds for the Central Universities (2014QNA4030).

References

[1] Y. Xu and C.W. Shu. Local discontinuous Galerkin methods for high-order time-dependent partial differential equation. Commun. Comput. Phys., 7:1-46, 2010.
[2] R. Camassa and D. Holm. An integrable shallow water equation with peaked solitons. Phys. Rev. Letter, 7:1661-1664, 1993.
[3] A. Constantin. Existence of permanent and breaking waves for a shallow water equation: a geometric approach. Ann. Inst. Fourier, Grenoble, 50:321-362, 2000.
[4] A. Parker. Binary cuspon-soliton interactions. Chaos Soliton Fract., 41:1531-1549, 2009.
[5] Y. Xu and C. W. Shu. A local discontinuous Galerkin method for the Camassa-Holm equation. SIAM J. Numer. Anal., 46(4):1998-2021, 2008.
[6] X. Liang, X. Li, D. Fu, Y. Ma. Complex transition of double-diffusive convection in a rectangular enclosure with hieght-to-length ratio equal to 4: Part I. Commun. Comput. Phys., 6(2):247-268, 2009.

[7] Y. T. Zhang and C. W. Shu. Third order WENO schemes on three dimensional tetrahedral meshes. Commun. Comput. Phys., 5:863-848, 2009.
[8] B. F. Feng, K. Maruno and Y. Ohta. A self-adaptive mesh method for the Camassa-Holm equation. J. Comput. Appl. Math., 235(1):229-424, 2010.
[9] H. Kalisch and J. Lenells. Numerical study of traveling-wave solutions for the Camassa-Holm equation. Chaos Soliton Fract., 25:287-298, 2005.
[10] R. Artebrant and H. J. Schroll. Numerical simulation of Camassa-Holm peakons by adaptive upwinding. Appl. Numer. Math., 56:695-711, 2006.
[11] D. Cohen, B. Owren and X. Raynaud. Multi-symplectic integration of the Camassa-Holm equation. J. Comput. Phys., 227:5492-5512, 2008.
[12] T. Matsuo and H. Yamaguchi. An energy-conserving Galerkin scheme for a class of nonlinear dispersive equations. J. Comput. Phys., 228:4346-4358, 2009.
[13] T. Matsuo. A Hamiltonian-conserving Galerkin scheme for the Camassa Holm equation.. J. Comput. Appl. Math., 234:1258-1266, 2010.
[14] D. D. Holm and M. F. Staley. Wave structure and nonlinear balances in a family of evolutionary PDEs. SIAM J. Appl. Dyn. Syst., 2:323-380, 2003.
[15] Y. Xu and C.W. Shu. Local discontinuous Galerkin methods for the Degasperis-Procesi equation. Commun. Comput. Phys., 10:474-508, 2011.
[16] B.F. Feng and Y. Liu. An operator splitting method for the Degasperis-Procesi equation. J. Comput. Phys., 228:7805-7820, 2009.
[17] T. J. Bridges and S. Reich. Multi-symplectic integrators: numerical schemes for Hamiltonian PDE that conserve symplecticity. Phys. Letter A, 284(4-5):184-193, 2001.
[18] M. Stanislavova and A. Stefanov. On global finite energy solutions of the Camassa-Holm equation. J. Fourier Anal. Appl., 11(5):511-53, 2005.
[19] P. H. Chiu, L. Lee and T. W. H. Sheu. A dispersion-relation-preserving algorithm for a nonlinear shallow-water wave equation. J. Comput. Phys., 228:8034-8052, 2009.
[20] T. W. H. Sheu, P. H. Chiu and C. H. Yu. On the development of a high-order compact scheme for exhibiting the switching and dissipative solution natures in the Camassa-Holm equation. J. Comput. Phys., 230:5399-5416, 2011.
[21] W. Oevel and W. Sofroniou. Symplectic Runge-Kutta schemes II: classification of symplectic method. Univ. of Paderborn, Germany, Preprint, 1997.
[22] T. K. Sengupta, M. K. Rajpoot and Y. G. Bhumkar. Space-time discretizing optimal DRP schemes for flow and wave propagation problems. Comput. Fluids, 47(1):144-154, 2011.
[23] T. K. Sengupta, V. V. S. N. Vijay and S. Bhaumik. Further improvement and analysis of CCD scheme: Dissipation discretization and de-aliasing properties. J. Comput. Phys., 228:6150-6168, 2009.
[24] T. Nihei and K. Ishii. A fast solver of the shallow water equations on a sphere using a combined compact difference scheme. J. Comput. Phys., 187:639-659, 2003.
[25] C. K. W. Tam and J. C. Webb. Dispersion-relation-preserving finite difference schemes for computational acoustics. J. Comput. Phys., 107:262-281, 1993.
[26] P. C. Chu and C. Fan. A three-point combined compact difference scheme. J. Comput. Phys., 140:370-399, 1998.
[27] A. Parker and Y. Matsuno. The peakon limits of soliton solutions of the Camassa-Holm equation. J. Phys. Soc. Japan, 75(12):124001, 2006.
[28] J. Lenells. Traveling wave solutions of the Camassa-Holm eqaution. J. Differen. Equat., 217:393-430, 2005.
[29] R. Camassa, D. D. Holm and J. M. Hyman. A new integrable shallow water equation. Adv.

Appl. Mech., 31:1-33, 1994.
[30] H. Holden and X. Raynaud. Global dissipative multipeakon solutions of the Camassa-Holm equation. Comm. Partial Differen. Equat., 33(11):2040-2063, 2008.
[31] G.S. Jiang and D. Peng. Weighted ENO schemes for Hamilton-Jacobi equations. SIAM J. Sci. Comput., 21:2126-2143, 2000.
[32] Y. Ohta, K I. Maruno and B. F. Feng. An integrable semi-discretization of the Camassa-Holm equation and its determinant solution. J. Phys. A: Math. Theor., 41:355205, 2008.